Engineering $SrSnO_3$ Phases and Electron Mobility at Room Temperature Using Epitaxial Strain

Tianqi Wang[1, *, †], Abhinav Prakash[1, *, †], Yongqi Dong[2, 3, 5], Tristan Truttmann[1], Ashley Bucsek[4], Richard James[4], Dillon D. Fong[2], Jong-Woo Kim[3], Philip J. Ryan[3], Hua Zhou[3], Turan Birol[1], and Bharat Jalan[1,*]

[1]Department of Chemical Engineering and Materials Science
University of Minnesota,
Minneapolis, Minnesota 55455, USA

[2]Materials Science Division, Argonne National Laboratory,
Argonne, Illinois 60439, USA

[3]Advanced Photon Source, Argonne National Laboratory,
Argonne, Illinois 60439, USA

[4]Department of Aerospace Engineering and Mechanics
University of Minnesota
Minneapolis, Minnesota 55455, USA

[5]National Synchrotron Radiation Laboratory, University of Science and Technology of China,
Hefei, Anhui 230026, China

† Equal contributing authors

[a)] Corresponding authors: wang3769@umn.edu, praka019@umn.edu, and bjalan@umn.edu

Abstract

High-speed electronics require epitaxial films with exceptionally high carrier mobility at room temperature. Alkaline-earth stannates with high room-temperature mobility show outstanding prospects for oxide electronics operating at ambient temperatures. However, despite significant progress over the last few years, mobility in stannate films has been limited by dislocations due to the inability to grow fully coherent films. Here, we demonstrate the growth of coherent, strain-engineered phases of epitaxial $SrSnO_3$ (SSO) films using a radical-based molecular beam epitaxy approach. Compressive strain stabilized the high-symmetry tetragonal phase of SSO at room temperature (RT), which, in bulk, exists only at temperatures between 1062 K and 1295 K. We achieved a mobility enhancement of over 300% in doped films compared with the low temperature orthorhombic polymorph. Using comprehensive temperature-dependent synchrotron-based X-ray measurements, electronic transport and first principles calculations, crystal and electronic structures of SSO films were investigated as a function of strain. We argue that strain-engineered films of stannate will enable high mobility oxide electronics operating at RT with the added advantage of being optically transparent.

Keywords

Hybrid molecular beam epitaxy, strain engineering, Octahedral rotations, high mobility, half-order diffraction, density functional theory, phase transition

Introduction

Strain-engineered semiconductor heterostructures have been studied for decades as a method to engineer the carrier mobility. A well-known example is the compressively strained channel in silicon-based field-effect transistors (FET) that has resulted in significant enhancement of electron/hole mobility.[1-5] Similar concepts have been investigated in the prototypical perovskite oxide semiconductor, La-doped $SrTiO_3$ (STO), where a fourfold enhancement in electron mobility has been realized at low temperatures.[6] However, at room-temperature (RT), STO possesses mobility of less than 10 cm^2/Vs. In contrast to STO, alkaline-earth stannates show significantly larger mobilities at RT, 320 cm^2/Vs in bulk doped-$BaSnO_3$ (BSO) and up to 180 cm^2/Vs in thin films.[7-13] Wide bandgap of stannates adds functionalities of optical transparency[14-15] and high electrical breakdown. However, strain engineering or even the growth of a coherent heteroepitaxial film has not been realized previously in the alkaline earth stannates. Attempts to grow strained BSO have failed due to the large lattice mismatch with commercially available substrates. Electron mobility in BSO films has therefore been mostly limited by dislocations at low carrier concentrations. On the other hand, $SrSnO_3$ (SSO) belongs to the same family of compounds and possesses smaller lattice parameters and has significant potential for strain and mobility engineering at RT. Furthermore, the wider bandgap of SSO (4 - 4.5 eV)[16-18] makes it an excellent candidate for transparent conductors, barrier layers in heterostructure engineering, and high-power electronic device applications.[19-21] Much concerning the electronic structure of SSO, however, remains elusive. This is largely due to the inability to grow conducting SSO films.[22]

Bulk SSO has four crystalline polymorphs – a room-temperature orthorhombic phase (*Pnma* with $a^-a^-c^+$ tilt pattern at $T \leq 905$ K), a high-temperature orthorhombic phase (*Imma* with

$a^-a^-c^0$ tilt pattern at 905 K ≤ T ≤1062 K), a high-temperature tetragonal phase (*I4/mcm* with $a^0a^0c^+$ tilt pattern at 1062 K ≤ T ≤ 1295 K) and the cubic phase (*Pm*$\bar{3}$*m* with $a^0a^0a^0$ tilt pattern at T ≥ 1295 K).[23] Tilt systems, represented using Glazer notation, are referenced with respect to the orthorhombic unit cell, where the tilt angles α, β, and γ of SnO_6 octahedron are defined along $[100]_{pc}$, $[010]_{pc}$ and $[001]_{pc}$ directions of the pseudocubic unit cell, respectively. (+) and (−) in the Glazer notation represents in-phase and out-of-phase tilts, respectively.[24-26]

The more symmetric tetragonal phase desirable for high mobility applications is stable only at elevated temperatures. The key scientific challenge is to stabilize higher symmetry phases at room temperature using the thin film architecture. First-principles calculations predict that phase stabilization may be possible using biaxial strain (see figure S1) but remains to be verified experimentally.[27]

Using a novel, radical-based molecular beam epitaxy (MBE) approach,[28-29] and through systematic control of epitaxial strain on different substrates, we have stabilized different polymorphs of SSO at RT in thin film form. We employ synchrotron x-ray scattering, electronic transport, and first-principles calculations to disentangle these phases, revealing over a three-fold increase in RT mobility under compressive strain owing to band structure modification, demonstrating the importance of strain engineering in oxide-based electronics.

In figures 1a and 1b, we show the pseudocubic unit cell of the orthorhombic crystal and the two possible configurations in which films can be grown commensurately on an underlying substrate. Figure 1c elucidates the tilt angles α, β, and γ of the SnO_6 octahedron defined with respect to the $[100]_{pc}$, $[010]_{pc}$ and $[001]_{pc}$ directions of the pseudocubic unit cell, respectively. The pseudocubic lattice parameters of SSO, a_{pc}, b_{pc}, and c_{pc} are defined as $a_{pc} = b_{pc} = \frac{\sqrt{a_o^2 + b_o^2}}{2}$,

and $c_{pc} = \frac{c_o}{2}$; where a_o, b_o, and c_o refer to the lattice parameters of the orthorhombic unit cell of SSO. We note that the pseudocubic unit cell of an orthorhombic structure results in a monoclinic symmetry with $a_{pc} = b_{pc} \neq c_{pc}$ and $\alpha_{pc} = \gamma_{pc} = 90° \neq \beta_{pc}$, where α_{pc}, β_{pc} and γ_{pc} are the interaxial angles of the pseudocubic unit cell.

Results and Discussion

We first discuss the structure of stoichiometric SSO films grown on different substrates. Figures 2a, 2c, and 2e show specular x-ray diffraction scans for the three heterostructures: 12 nm La-doped SSO/2 nm SSO/$GdScO_3$ (GSO) (110), 43 nm La-doped SSO/9 nm SSO/$PrScO_3$ (PSO) (110), and 4 nm BSO/15 nm SSO/53 nm BSO/STO (001), respectively. These results reveal the synthesis of phase-pure films with an expanded out-of-plane lattice parameter (a_{op}) of 4.114 Å ± 0.002 Å, 4.058 ± 0.002 Å and 4.010 Å ± 0.002 Å for films grown on GSO (110), PSO (110) and BSO-buffered STO (001), respectively. It is noted that the BSO film on STO (001) is mostly relaxed with in-plane lattice parameters of 4.095 Å. For the rest of the discussion, we will refer to BSO-buffered STO (001) as simply BSO (001). Synchrotron x-ray scattering was employed to obtain the corresponding three-dimensional reciprocal space maps (RSMs) shown in figures 2b, 2d, and 2f. These depict non-specular RSMs of SSO films measured at the $(103)_{pc}$, $(013)_{pc}$, $(0\bar{1}3)_{pc}$, and $(\bar{1}03)_{pc}$ film reflections adjacent to similar substrate Bragg reflections in the pseudocubic GSO (110), PSO (110), and STO (001), respectively. The RSMs show that the films possess the same in-plane lattice parameters as that of the substrate represented by q_x and q_y in the reciprocal space. The SSO films are therefore epitaxial and coherently-strained to the substrate as well as phase-pure. Finite-size thickness fringes are also observed, indicating that the films have sharp interfaces on short lateral length scales irrespective of the choice of substrates.

Inspection of the q_z values for the *substrate* diffraction peaks in figures 2b and 2d reveal identical values for $(013)_{pc}$ and $(0\bar{1}3)_{pc}$ diffraction peaks, but different values for $(103)_{pc}$ and $(\bar{1}03)_{pc}$ peaks, respectively, indicating monoclinic symmetry for the pseudocubic unit cell of GSO (110) and PSO (110). A similar trend with a much smaller difference between q_z values for the $(103)_{pc}$ and $(\bar{1}03)_{pc}$ *film* reflections was also observed (dashed horizontal lines in figure 2b and 2d), suggesting a *non-negligible* monoclinic distortion in SSO grown on GSO (110) and PSO (110). On the other hand, the q_z values for diffraction peaks in figure 2f are identical for all peaks, suggesting four-fold tetragonal symmetry for the SSO film grown on BSO (001).

The expected values of a_{op} for fully coherent polymorphs of SSO on GSO (110), PSO (110) and BSO (001), are provided in Table S1 (See Supporting Information), assuming c_{pc} is oriented either in-plane or out-of-plane with respect to the substrate, as illustrated in figures 1a and 1b, respectively. To calculate a_{op}, we used theoretical values of elastic constants while ignoring thermal expansion.[30] The calculated a_{op} values are used only as a guide for identifying different polymorphs based on the measured lattice parameters. The experimental $a_{op,}$ 4.114 Å ± 0.002 Å for the SSO film on GSO (110), is close to the calculated values of 4.111 Å and 4.119 Å (see Table S1) for the high-temperature orthorhombic and tetragonal SSO polymorphs, respectively, suggesting that either a high-temperature orthorhombic or a tetragonal phase is stabilized on GSO (110) substrates. Similarly, the SSO film grown on PSO (110) exhibits an experimental a_{op} value of 4.058 ± 0.002 Å, suggestive of either the RT orthorhombic (4.038 Å) or high-temperature orthorhombic (4.085 Å) polymorphs of SSO. For the SSO film grown on a BSO (001), a_{op} = 4.010 Å ± 0.002 Å, which is remarkably close to the value for the RT orthorhombic phase (see table S1). Therefore, the identification of polymorphic phases based on

the lattice parameter alone is non-trivial. We employ temperature-dependent x-ray diffraction to distinguish these phases.

Figure 3a shows specular x-ray diffraction scans for a representative 30 nm La-doped SSO/2 nm SSO/GSO (110) around the (002) reflection at 10 K and 300 K. Note that this film had an identical lattice parameter to that of 12 nm La-doped SSO/2 nm SSO/GSO (110) (figure S2). A distinct film peak accompanied by a significantly smaller lattice parameter was observed at 10 K suggesting a structural phase transition on cooling. To obtain further insights into the phase transition, we performed temperature-dependent diffraction at half-order reflections. These reflections originate from tilts/rotations in the octahedral network.[24, 31] Figures 3b-d show half-order diffraction scans around (1 $^1/_2$ $^5/_2$), ($^1/_2$ $^1/_2$ $^5/_2$), and ($^3/_2$ $^1/_2$ $^3/_2$) reflections recorded at 10 K and 300 K. For brevity, details of the half-order diffraction analyses are described in the supporting information. Scans at 300 K in figures 3b and 3c revealed a broad film peak with nearly zero intensity around the (1 $^1/_2$ $^5/_2$), and ($^1/_2$ $^1/_2$ $^5/_2$) reflections, whereas a significantly more intense peak (figure 3d) was observed around the ($^3/_2$ $^1/_2$ $^3/_2$) reflection. Half-order Bragg peak analysis of this SSO film, therefore, yields $a^0a^0c^-$ tilt pattern with the "broad and less intense" peaks being consistent with a small monoclinic distortion associated with the strained orthorhombic structure also suggested by RSMs in figure 2b. Based on the rotational symmetry and measured a_{op}, this result confirms a high-temperature tetragonal phase of SSO film on GSO (110) at 300 K was confirmed. At 10 K, significantly stronger in-phase (+) and out-of-phase (−) rotations were observed along $[100]_{pc}$ and $[010]_{pc}$, respectively as evidenced by the intense peak around (1 $^1/_2$ $^5/_2$), and ($^1/_2$ $^1/_2$ $^5/_2$) reflections. These half-order diffraction scans were also accompanied by the finite-size thickness fringes, corresponding to the

film thickness of 32 nm. On the other hand, out-of-phase (−) rotation along the $[001]_{pc}$ remained nominally unchanged. We, therefore, conclude a $a^+b^-c^-$ tilt pattern at 10 K. This is consistent with the RT orthorhombic phase of SSO, where $[001]_O$ of the film is in-plane with respect to the substrate, as illustrated in figure 1a. No in-phase (+) rotation was observed in the $[001]_{pc}$ direction revealing single domain films.[32] This observation attests to the excellent structural quality of these films and reveals that the a^+ and b^- rotations are spread over the entire film thickness at 10 K. In this context, it is important to note that the broad half-order diffraction peaks at 300 K in figure 3b and 3c are likely associated with the substrate-induced distortion in the SSO layers adjacent to the film/substrate interface. In comparison to this film grown on GSO (110), which provided biaxial compressive strain, films grown on PSO (110) (nearly zero mismatch) and BSO (001) (biaxial tension) did not show any *T*-dependent phase transition down to 10 K as shown in figures S3 and S4, respectively. A similar analyses of half-order Bragg peaks of the SSO film on PSO (110) yielded $a^+b^-c^-$ tilt pattern with no measurable difference between 300 K and 10 K (figure S3). Additionally, the results on PSO (110) showed similar finite-size thickness fringes, suggesting $a^+b^-c^-$ rotations are spread over the entire film thickness. This rotational symmetry is consistent with the RT orthorhombic phase of SSO when the film is grown on PSO (110), where $[001]_O$ of the film is in-plane with respect to the substrate as illustrated in figure 1a. The absence of in-phase (+) rotation observed in the $[001]_{pc}$ direction imply single domain films on PSO (110) as well. Our analyses of the half-order diffraction patterns of the SSO film on BSO (001) (not shown) did not reveal any conclusive information on rotation patterns. However, combining the absence of phase transition as a function of temperature (figure S4), and the measured out-of-plane lattice parameter of film as depicted in figure 2e, we suggest that a RT orthorhombic phase of SSO stabilizes on BSO (001). These

results of phase stabilization agree with the phases predicted by our DFT calculations (figure S1).

To investigate the nature of the phase transition in the 30 nm La-doped SSO/2 nm SSO/GSO (110) film, we performed temperature-dependent x-ray diffraction. We also conducted electronic transport measurements as a more sensitive measure for determining the onset and completion of phase transition using the same sample. Figure 4a shows a_{op} as a function of temperature between 100 K ≤ T ≤ 280 K clearly indicating a first order transition. Individual scans as function of temperature for the (002) film reflection revealing the evolution of the tetragonal phase with increasing temperature from 100 K to 280 K is included in the supporting information (figure S5). These results thus indicate that the two phases coexist at temperatures between 180 K and 280 K. Figure S5 further reveals that the two phases are present in equal fraction at 240 K ≤ T ≤ 250 K (also marked by an orange arrow in figure 4a). To put the significance of this result in perspective, the first order phase transition in bulk SSO occurs at ~1062 K revealing over 800 K reduction in the phase transition temperature (T_c) using moderate biaxial strain. To the best of our knowledge, this is the *highest* reported change in T_c using epitaxial strain among all materials studied to date. To explain this large suppression in phase transition temperature, we propose a qualitative scheme as discussed in the supporting material (figure S6).[33-34]

Figure 4b and 4c show the temperature dependence of resistivity (ρ) and its first derivative with respect to temperature ($d\rho/dT$), respectively, for the same sample on GSO (110) upon heating and cooling. Apparent kinks were observed around 180 K and 285 K (marked by black arrows). These two arrows mark the temperatures at which the onset and the completion of phase transition occur on heating, respectively. The slope of the resistivity curve $d\rho/dT$ vs. T

further reveals small but non-negligible thermal hysteresis (ΔT). Identical values of ΔT = ~ 13.0 K and ΔT = ~ 0.3 K was observed in two cycles near the lower (180 K) and upper boundary (~285 K) of the phase transition, respectively. No measurable difference in the value of resistivity (ρ) between the two cycles, except around the onset/completion of phase transition, suggests a reversible phase transition.

We now discuss the electronic properties of these phases. We performed temperature-dependent electronic transport measurements along with the DFT-based calculations. Figures 5a-c show the temperature dependence of ρ, 3D carrier density (n), and mobility (μ), respectively, for a representative 40-43 nm-thick La-doped SSO films grown with 8-9 nm undoped buffer layer on GSO (110) and PSO (110). For a one-to-one comparison, the La dopant concentration was kept constant (~ 0.5 at.%) by maintaining a fixed La effusion cell temperature (1150 °C) and growth rate. The RT orthorhombic polymorph (SSO on PSO (110)) yielded room-temperature values of $\rho = 5.1 \times 10^{-3}$ Ω-cm, and $\mu = 17$ $cm^2V^{-1}s^{-1}$ at $n = 7.1 \times 10^{19}$ cm^{-3}, whereas tetragonal polymorphs under compressive strain (SSO on GSO (110)) resulted in over a *threefold* enhancement in $\mu = 55$ $cm^2V^{-1}s^{-1}$, accompanied by ~30% decrease in $n = 4.2 \times 10^{19}$ cm^{-3}, resulting in an overall lower $\rho = 2.2 \times 10^{-3}$ Ω-cm. To gain deeper insight into the electronic band structures of the RT orthorhombic and high-temperature tetragonal polymorphs, we performed DFT calculations of the electronic band structures of these phases constrained to the substrate with biaxial strain. No considerations of symmetry/octahedral rotation mismatch were made in the DFT calculations. Figure 5d shows the calculated *E-k* diagram for two SSO phases – the RT orthorhombic and high-temperature tetragonal phase revealing a lower electron effective mass, 0.3141 m_e, along both the k_x and k_y directions for the tetragonal polymorph, whereas the RT orthorhombic phase showed about 30% higher values, 0.4075 m_e and 0.3947 m_e along k_x and k_y,

respectively. The projection of the energy surface on the $k_y - k_x$ plane for the RT orthorhombic phase is shown in figure 5d, which also revealed a small, anisotropic electron effective mass along the k_x and k_y directions. While the enhancement in mobility can be due to lowering of the electron effective mass in the tetragonal phase, it does not explain the *threefold* increase. This result thus suggests additional factors could be responsible for the increased electron mobility in the tetragonal phase, such as reduced defect scattering and/or changes in the phonon band structure that affects the electron-phonon scattering. Furthermore, the DFT calculations revealed no measurable change in the bandgap, raising a question on the origin of change in carrier density. We hypothesize that this is either due to a small change in the density of states at the Fermi level or a change in the ionization energy of dopant atoms in two phases. Future investigations should be conducted to examine the dielectric constant, mobility scattering mechanisms, the dopant solubility, and the dopant activation energy in these polymorphs.

Conclusion

In summary, we have demonstrated over a *threefold* increase in electron mobility at room temperature in compressively strained SSO films as compared to nominally unstrained SSO films. Strain engineering results in the stabilization of different polymorphs of SSO at room temperature. A compressive strain of -2.6% results in a first-order phase transition accompanied by the giant reduction in transition temperature by ~ 800 K. Nearly zero strain and tensile strain stabilize the RT orthorhombic phase. The results point to a wide range of opportunities available to tailor high-mobility oxide heterostructure properties through doping, strain and phase optimization, paving ways to explore oxide electronics at room temperature.

Methods

I. MBE Growth, doping and characterization of $SrSnO_3$ films:

A radical-based MBE approach was employed to grow SSO films on GSO (110), PSO (110), and BSO-buffered STO (001) substrates using an oxide MBE system (EVO 50, Omicron Nano Technology, Germany) with a base pressure of 10^{-10} Torr. Details of our MBE approach for stannate film growth are discussed elsewhere.[19] A brief description will be provided here. SSO films were grown via hybrid MBE. Hexamethylditin (HMDT) was used as the metal-organic chemical precursor for Sn.[28] Sr (99.99 %, Sigma-Aldrich) and La were evaporated using effusion cells, and oxygen was supplied using an RF plasma source. The oxygen pressure and substrate temperature were fixed at 5×10^{-6} Torr and 900 °C (thermocouple temperature), respectively for all growths. Prior to the film growth, substrate surface was cleaned using oxygen plasma for 20 min. SSO films were grown by co-depositing Sr, HMDT and oxygen. Reflection high-energy electron diffraction (RHEED) (Staib Instruments, Germany) was utilized to monitor the growth *in-situ*.

Ex situ structural characterization was performed in a high-resolution Philips Panalytical X'Pert thin-film diffractometer using Cu K_α radiation. Synchrotron-based x-ray diffraction was performed at the Advanced Photon Source (APS), Argonne National Laboratory. Reciprocal space maps were collected at sector 12-ID-D of the APS. The x-ray beam at sector 12-ID-D had an average flux of 2×10^{12} photons/s at the wavelength of 0.6199 Å and a beam profile of 0.2 (V) × 1 (H) mm^2. A 6-circle Huber high-resolution x-ray diffractometer was used to perform line scans and reciprocal space mapping (both 00L specular and HKL non-specular scans) to extract the out-of-plane and in-plane lattice parameters of $SrSnO_3$ films. To gain information about the

symmetry and octahedral rotation patterns of films, temperature-dependent half-order (*hkl*) diffraction scans were performed at sector 6-ID-B,C of the APS.

La was used as a *n*-type dopant for SSO films. As grown La-doped SSO films were annealed in oxygen *ex-situ* using rapid thermal annealer at 800 °C for 2 min to minimize contribution from the residual oxygen vacancies to the electronic transport. All substrates after film growth and undoped films were insulating ($\rho > 10^5$ Ω-cm). Transport measurements were performed in the van der Pauw geometry using a Physical Property Measurement System (Quantum Design Dynacool, USA) between 1.8 K and 300 K. A field sweeps of - 9 T to + 9 T was used for the hall measurements.

DFT Calculation Details:

First principles calculations were performed using the Projector Augmented Wave (PAW) method as implemented in The Vienna Ab Initio Simulation Package (VASP).[35-36] PBEsol approximation, which is known to provide good lattice constants for oxides, was used to approximate the exchange correlation.[37] A shifted *k*-point grid of 8×8×8 for the primitive perovskite cell, which corresponds to roughly a *k*-point per ~0.015 $Å^{-1}$, was employed,[38] along with a cut-off energy of 500 eV for the plane-waves. Spin-orbit coupling was not considered in the relaxation of the crystal structures. Its effect on the band structure was seen to be minimal and was ignored in the effective mass calculations either. When searching for the ground state under biaxial strain boundary conditions, the out-of-plane lattice parameter was allowed to relax to optimize the energy, however, the change of the monoclinic angle (which is shown to be close to 90°) was not considered. To ensure that the structure does not get stuck in a local energy minimum, some of the calculations for complex tilt patters and low symmetry were repeated with different starting points.

Data availability

The data that supports the main findings of this study are available from the corresponding authors on request.

Author Contributions

B.J., T.W., and A.P. conceived and designed the experiments; T.W. and A.P. grew the sample, measured and analyzed the structural and transport data; P.J.R., H.Z., A.P., Y.D., J.-W.K., T.T, and D.D.F. carried out synchrotron-based x-ray diffraction measurements and analyses; T.B. conducted the DFT calculation; A.B. and R.J. provided the theoretical model for the change in phase transition temperature, and all authors contributed to the scientific discussion and wrote the manuscript.

Associated Content

Supporting Information is available free of charge on the ACS Publication website at DOI: <insert URL>

Phase stability diagram calculated using DFT, expected lattice parameters for fully-coherent films, temperature dependent x-ray diffraction, and qualitative description of large suppression in phase transition temperature.

Notes: The authors declare no competing financial interests.

Acknowledgements

This work was primarily supported by National Science Foundation through DMR-1741801 and DMR-1607318, and partially by the UMN MRSEC program under Award No. DMR-1420013.

Part of this work was supported through the Young Investigator Program of the Air Force Office of Scientific Research (AFOSR) through Grant No. FA9550-16-1-0205. The work also acknowledges partial support from the RDF Fund of the Institute on the Environment (UMN). Parts of this work were carried out at the Minnesota Nano Center and Characterization Facility, University of Minnesota, which receives partial support from NSF through the MRSEC program. T.W. and A.P. would like to acknowledge the support from the UMN Doctoral Dissertation Fellowships. Use of the Advanced Photon Source, an Office of Science User Facility operated for the U.S. Department of Energy (DOE) Office of Science by Argonne National Laboratory, was supported by the U.S. DOE under Contract No. DE-AC02-06CH11357.

References

1. Welser, J., NMOS and PMOS Transistors Fabricated in Strain Silicon/Relaxed Silicon-Germanium Structures. *IEDM Tech. Dig.* **1992**.
2. Höck, G.; Kohn, E.; Rosenblad, C.; von Känel, H.; Herzog, H. J.; König, U., High Hole Mobility in $Si_{0.17}Ge_{0.83}$ Channel Metal–Oxide–Semiconductor Field-Effect Transistors Grown by Plasma-Enhanced Chemical Vapor Deposition. *Appl. Phys. Lett.* **2000,** *76* (26), 3920.
3. Lee, M. L.; Leitz, C. W.; Cheng, Z.; Pitera, A. J.; Langdo, T.; Currie, M. T.; Taraschi, G.; Fitzgerald, E. A.; Antoniadis, D. A., Strained Ge Channel p-type Metal–Oxide–Semiconductor Field-Effect Transistors Grown on $Si_{1-x}Ge_x$/Si Virtual Substrates. *Appl. Phys. Lett.* **2001,** *79* (20), 3344.
4. Lee, M. L.; Fitzgerald, E. A., Hole Mobility Enhancements in Nanometer-Scale Strained-Silicon Heterostructures Grown on Ge-rich Relaxed $Si_{1-x}Ge_x$. *J. Appl. Phys.* **2003,** *94* (4), 2590.
5. Lee, M. L.; Fitzgerald, E. A.; Bulsara, M. T.; Currie, M. T.; Lochtefeld, A., Strained Si, SiGe, and Ge Channels for High-Mobility Metal-Oxide-Semiconductor Field-Effect Transistors. *J. Appl. Phys.* **2004,** *97* (1), 011101.
6. Jalan, B.; Allen, S. J.; Beltz, G. E.; Moetakef, P.; Stemmer, S., Enhancing the Electron Mobility of $SrTiO_3$ with Strain. *Appl. Phys. Lett.* **2011,** *98* (13), 132102.
7. Luo, X.; Oh, Y. S.; Sirenko, A.; Gao, P.; Tyson, T. A.; Char, K.; Cheong, S. W., High Carrier Mobility in Transparent $Ba_{1-x}La_xSnO_3$ Crystals with a Wide Band Gap. *Appl. Phys. Lett.* **2012,** *100* (17), 172112.
8. Kim, H. J.; Kim, U.; Kim, H. M.; Kim, T. H.; Mun, H. S.; Jeon, B.-G.; Hong, K. T.; Lee, W.-J.; Chanjong, J.; Kim, K. H.; Char, K., High Mobility in a Stable Transparent Perovskite Oxide. *Appl. Phys. Express* **2012,** *5* (6), 061102.
9. Kim, H. J.; Kim, U.; Kim, T. H.; Kim, J.; Kim, H. M.; Jeon, B.-G.; Lee, W.-J.; Mun, H. S.; Hong, K. T.; Yu, J.; Char, K.; Kim, K. H., Physical Properties of Transparent Perovskite Oxides (Ba,La)SnO_3 with High Electrical Mobility at Room Temperature. *Phys. Rev. B* **2012,** *86* (16), 165205.
10. Prakash, A.; Xu, P.; Faghaninia, A.; Shukla, S.; Ager Iii, J. W.; Lo, C. S.; Jalan, B., Wide Bandgap $BaSnO_3$ Films with Room Temperature Conductivity Exceeding 10^4 Scm^{-1}. *Nat. Commun.* **2017,** *8*, 15167.
11. Raghavan, S.; Schumann, T.; Kim, H.; Zhang, J. Y.; Cain, T. A.; Stemmer, S., High-mobility $BaSnO_3$ Grown by Oxide Molecular Beam Epitaxy. *APL Mater.* **2016,** *4* (1), 016106.
12. Paik, H.; Chen, Z.; Lochocki, E.; H., A. S.; Verma, A.; Tanen, N.; Park, J.; Uchida, M.; Shang, S.; Zhou, B.-C.; Brützam, M.; Uecker, R.; Liu, Z.-K.; Jena, D.; Shen, K. M.; Muller, D. A.; Schlom, D. G., Adsorption-controlled growth of La-doped $BaSnO_3$ by molecular-beam epitaxy. *APL Mater.* **2017,** *5* (11), 116107.
13. Ganguly, K.; Prakash, A.; Jalan, B.; Leighton, C., Mobility-electron Density Relation Probed via Controlled Oxygen Vacancy Doping in Epitaxial $BaSnO_3$. *APL Mater.* **2017,** *5* (5), 056102.
14. Chambers, S. A.; Kaspar, T. C.; Prakash, A.; Haugstad, G.; Jalan, B., Band Alignment at Epitaxial $BaSnO_3/SrTiO_3$(001) and $BaSnO_3/LaAlO_3$(001) Heterojunctions. *Appl. Phys. Lett.* **2016,** *108* (15), 152104.

15. Arezoomandan, S.; Prakash, A.; Chanana, A.; Yue, J.; Mao, J.; Blair, S.; Nahata, A.; Jalan, B.; Sensale-Rodriguez, B., THz Characterization and Demonstration of Visible-transparent/terahertz-functional Electromagnetic Structures in Ultra-conductive La-doped $BaSnO_3$ Films. *Sci. Rep.* **2018,** *8* (1), 3577.
16. Mizoguchi, H.; Eng, H. W.; Woodward, P. M., Probing the Electronic Structures of Ternary Perovskite and Pyrochlore Oxides Containing Sn^{4+} or Sb^{5+}. *Inorg. Chem.* **2004,** *43* (5), 1667.
17. Singh, D. J.; Xu, Q.; Ong, K. P., Strain Effects on the Band Gap and Optical Properties of Perovskite $SrSnO_3$ and $BaSnO_3$. *Appl. Phys. Lett.* **2014,** *104* (1), 011910.
18. Gao, Q.; Chen, H.; Li, K.; Liu, Q., Band Gap Engineering and Room-Temperature Ferromagnetism by Oxygen Vacancies in $SrSnO_3$ Epitaxial Films. *ACS Appl. Mater. Inter.* **2018,** *10* (32), 27503.
19. Wang, T.; Thoutam, L. R.; Prakash, A.; Nunn, W.; Haugstad, G.; Jalan, B., Defect-driven Localization Crossovers in MBE-grown La-doped $SrSnO_3$ Films. *Phys. Rev. Mater.* **2017,** *1* (6), 061601.
20. Baba, E.; Kan, D.; Yamada, Y.; Haruta, M.; Kurata, H.; Kanemitsu, Y.; Shimakawa, Y., Optical and Transport Properties of Transparent Conducting La-doped $SrSnO_3$ Thin Films. *J. Phys. D Appl. Phys.* **2015,** *48* (45), 455106.
21. Ismail-Beigi, S.; Walker, F. J.; Cheong, S.-W.; Rabe, K. M.; Ahn, C. H., Alkaline Earth Stannates: The Next Silicon? *APL Mater.* **2015,** *3* (6), 062510.
22. Schumann, T.; Raghavan, S.; Ahadi, K.; Kim, H.; Stemmer, S., Structure and Optical Band Gaps of (Ba,Sr)SnO_3 Films Grown by Molecular Beam Epitaxy. *J. Vac. Sci. Technol. A* **2016,** *34* (5), 050601.
23. Glerup, M.; Knight, K. S.; Poulsen, F. W., High Temperature Structural Phase Transitions in $SrSnO_3$ Perovskite. *Mater. Res. Bull.* **2005,** *40* (3), 507.
24. Glazer, A. M., Simple Ways of Determining Perovskite Structures. *Acta Cryst. A* **1975,** *31* (6), 756.
25. Woodward, P., Octahedral Tilting in Perovskites. I. Geometrical Considerations. *Acta Cryst. B* **1997,** *53* (1), 32.
26. Woodward, P., Octahedral Tilting in Perovskites. II. Structure Stabilizing Forces. *Acta Cryst. B* **1997,** *53* (1), 44.
27. Ong, K. P.; Fan, X.; Subedi, A.; Sullivan, M. B.; Singh, D. J., Transparent Conducting Properties of $SrSnO_3$ and $ZnSnO_3$. *APL Mater.* **2015,** *3* (6), 062505.
28. Prakash, A.; Dewey, J.; Yun, H.; Jeong, J. S.; Mkhoyan, K. A.; Jalan, B., Hybrid Molecular Beam Epitaxy for the Growth of Stoichiometric $BaSnO_3$. *J. Vac. Sci. Technol. A* **2015,** *33* (6), 060608.
29. Prakash, A.; Xu, P.; Wu, X.; Haugstad, G.; Wang, X.; Jalan, B., Adsorption-controlled Growth and the Influence of Stoichiometry on Electronic Transport in Hybrid Molecular Beam Epitaxy-grown $BaSnO_3$ Films. *J. Mater. Chem. C* **2017,** *5* (23), 5730.
30. Ghebouli, B.; Ghebouli, M. A.; Chihi, T.; Fatmi, M.; Boucetta, S.; Reffas, M., First-principles Study of Structural, Elastic, Electronic and Optical Properties of $SrMO_3$ (M=Ti and Sn). *Solid State Commun.* **2009,** *149* (47), 2244.
31. May, S. J.; Kim, J. W.; Rondinelli, J. M.; Karapetrova, E.; Spaldin, N. A.; Bhattacharya, A.; Ryan, P. J., Quantifying Octahedral Rotations in Strained Perovskite Oxide Films. *Phys. Rev. B* **2010,** *82* (1), 014110.

32. Gao, R.; Dong, Y.; Xu, H.; Zhou, H.; Yuan, Y.; Gopalan, V.; Gao, C.; Fong, D. D.; Chen, Z.; Luo, Z.; Martin, L. W., Interfacial Octahedral Rotation Mismatch Control of the Symmetry and Properties of $SrRuO_3$. *ACS Appl. Mater. Inter.* **2016,** *8* (23), 14871-14878.
33. Ball, J. M.; James, R. D., Fine Phase Mixtures as Minimizers of Energy. *Arch. Ration. Mech. An.* **1987,** *100* (1), 13.
34. Bhattacharya, K.; James, R. D., A Theory of Thin Films of Martensitic Materials with Applications to Microactuators. *J. Mech. Phys. Solids.* **1999,** *47* (3), 531.
35. Kresse, G.; Hafner, J., Ab Initio Molecular Dynamics for Liquid Metals. *Phys. Rev. B* **1993,** *47* (1), 558.
36. Blöchl, P. E., Projector Augmented-Wave Method. *Phys. Rev. B* **1994,** *50* (24), 17953.
37. Perdew, J. P.; Burke, K.; Ernzerhof, M., Generalized Gradient Approximation Made Simple. *Phys. Rev. Lett.* **1996,** *77* (18), 3865.
38. Monkhorst, H. J.; Pack, J. D., Special Points for Brillouin-zone Integrations. *Phys. Rev. B* **1976,** *13* (12), 5188.

Figures (color online):

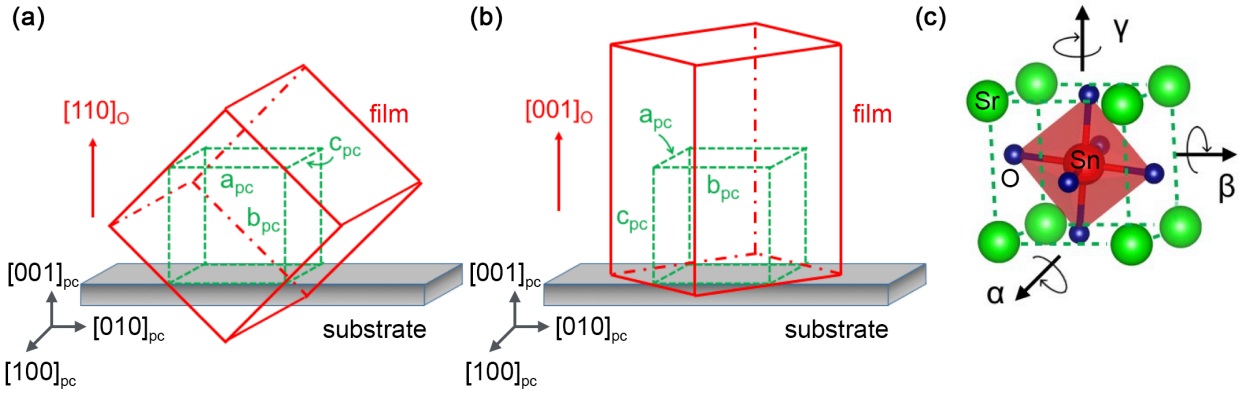

Figure 1: **$SrSnO_3$ unit cell**. Schematic of the pseudocubic unit cell (shown as green dotted lines) of an orthorhombic crystal structures (shown as red lines) illustrating two possible epitaxial relationships when films grow on a substrate - c_{pc} is (a) in-plane, and (b) out-of-plane with respect to the substrate; (c) the pseudocubic unit cell of SSO film showing SnO_6 octahedron with tilt angles α, β, and γ along $[100]_{pc}$, $[010]_{pc}$, and $[001]_{pc}$, respectively.

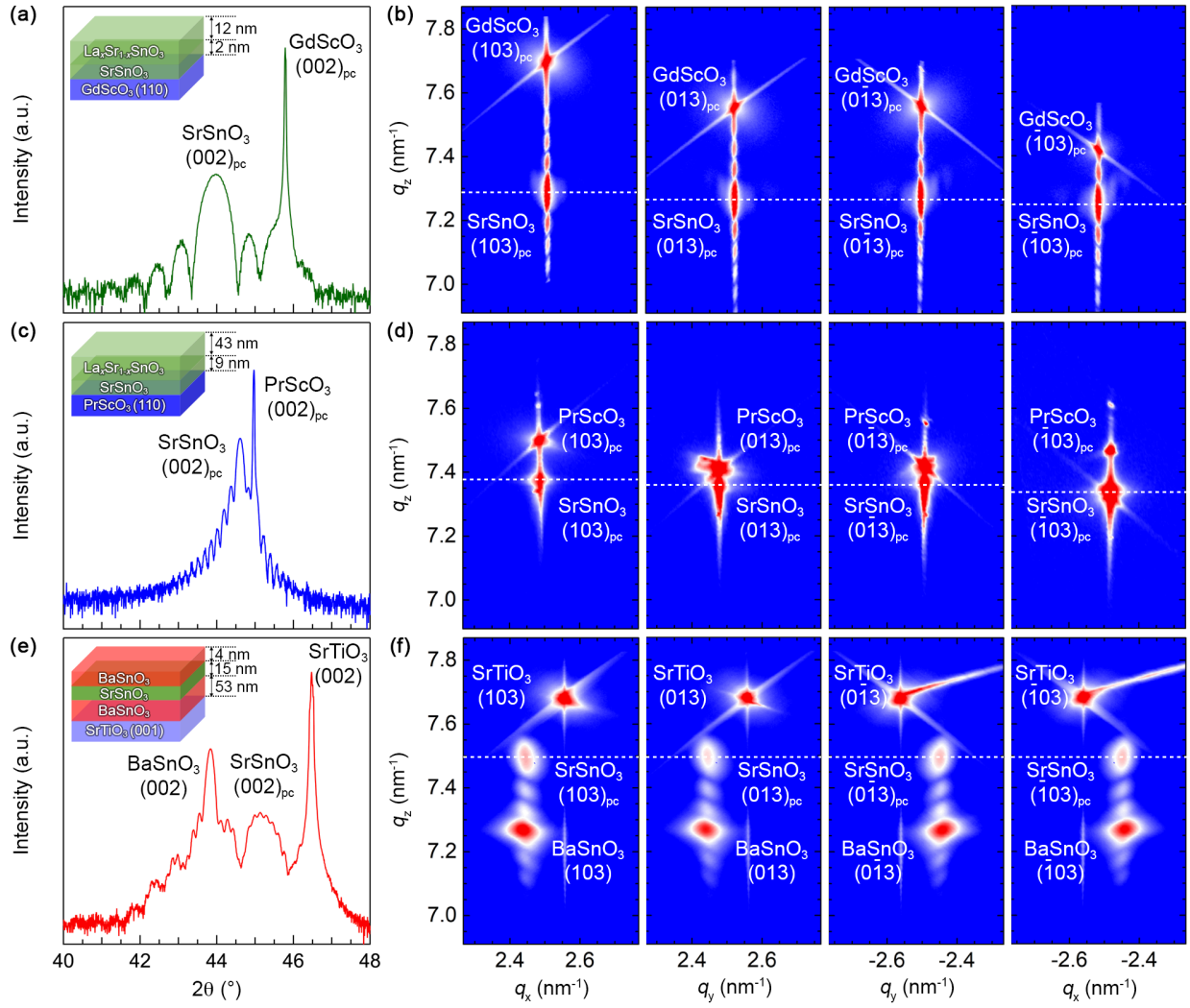

Figure 2: **Room-temperature x-ray diffraction**. (a,c,e) Wide-angle x-ray diffraction 2θ-ω scans for $SrSnO_3$ films grown on $GdScO_3$ (110), $PrScO_3$ (110), and $BaSnO_3$ (001)-buffered $SrTiO_3$ (001) substrates, respectively. Insets show schematics of these samples along with layer thicknesses. (b,d,f) Corresponding synchrotron-based non-specular reciprocal space maps of these samples around $(103)_{pc}$, $(013)_{pc}$, $(0\bar{1}3)_{pc}$, and $(\bar{1}03)_{pc}$ reflections. White dotted lines mark the position of the scattering vector (q_z) normal to the film surface indicating small monoclinic distortions in $SrSnO_3$ film in (b) and (d) but no distortion in (f). For all the scans, intensity was plotted on logarithmic scales.

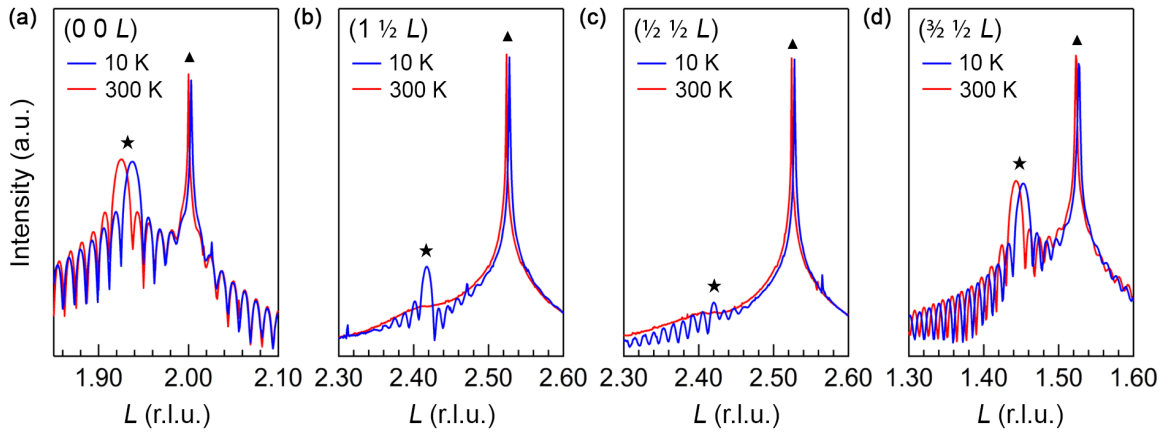

Figure 3: **Temperature-dependent x-ray diffraction**. Wide-angle x-ray diffraction scans of a 30 nm $La_xSr_{1-x}SnO_3$/2nm $SrSnO_3$ film grown on GSO (110) around (a) (0 0 2), (b) (1 $^1/_2$ $^5/_2$), (c) ($^1/_2$ $^1/_2$ $^5/_2$), and (d) ($^3/_2$ $^1/_2$ $^3/_2$) reflections at 300 K (red) and 10 K (blue) respectively, showing a phase transition from tetragonal ($a^0a^0c^-$) to orthorhombic ($a^+b^-c^-$) upon cooling. The GSO substrate and SSO film reflections are marked by ▲ and ⋆ symbols, respectively.

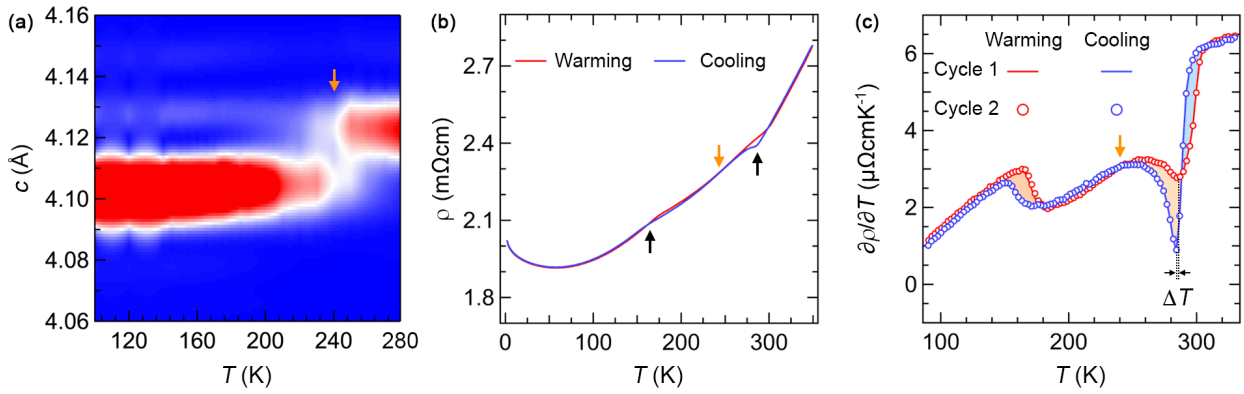

Figure 4: **First-order phase transition**. (a) Out-of-plane lattice parameter of a 30 nm $La_xSr_{1-x}SnO_3$/2nm $SrSnO_3$ film on GSO (110) as a function of temperature showing a first-order phase transition. (b) Temperature dependent resistivity (ρ) of the same film during warming and cooling cycles (2 K → 300 K → 2 K). Black arrows at 180 K and 285 K mark the onset and the completion of phase transition. (c) First derivative of ρ ($d\rho/dT$) as a function of T for the two cycles.

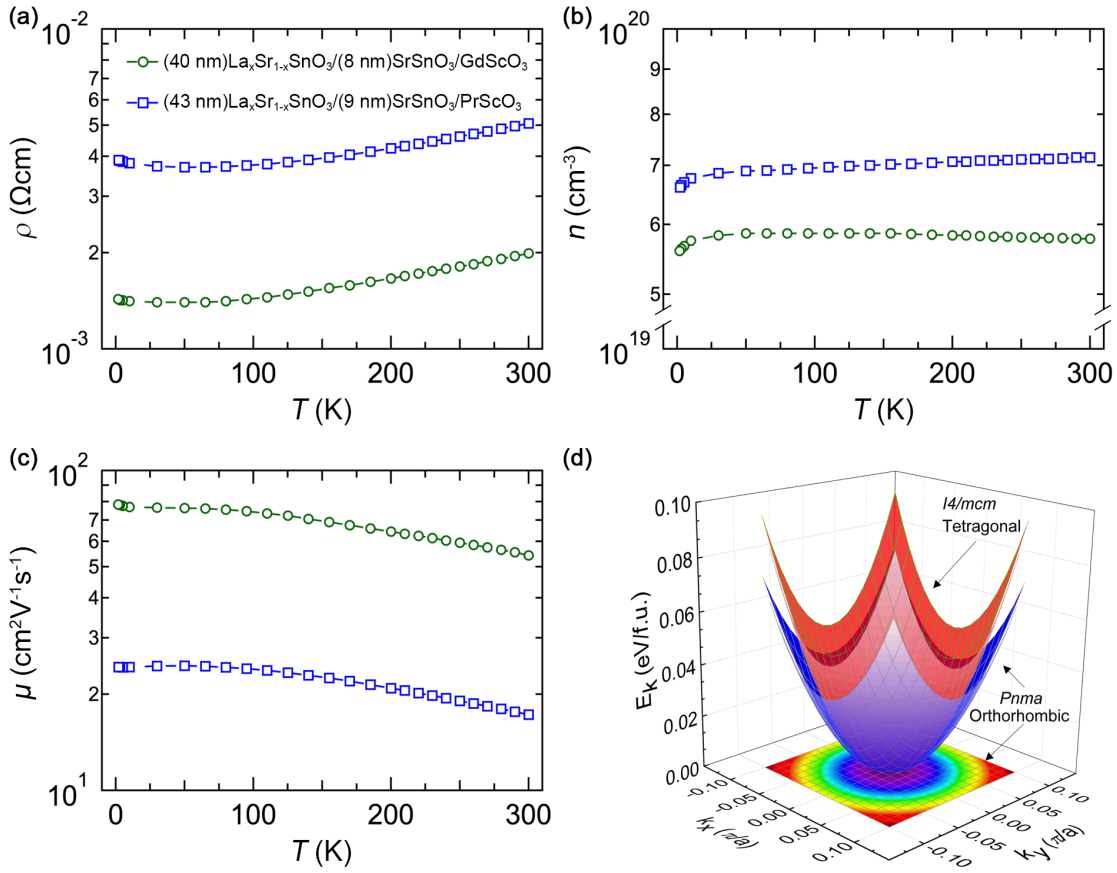

Figure 5: **Electronic properties of $SrSnO_3$ phases**. Temperature-dependence of (a) ρ, (b) carrier concentration (n), and (c) mobility (μ) for La-doped SSO films grown on GSO (110) and PSO (110). (d) Calculated dispersion relationship near the conduction band minima at Γ point for the tetragonal (red) and room-temperature orthorhombic (blue) phases of $SrSnO_3$ on $GdScO_3$ and $PrScO_3$, respectively. Two-dimensional projection of the energy surface of the room-temperature orthorhombic polymorph on the k_x - k_y plane is also shown.

TOC

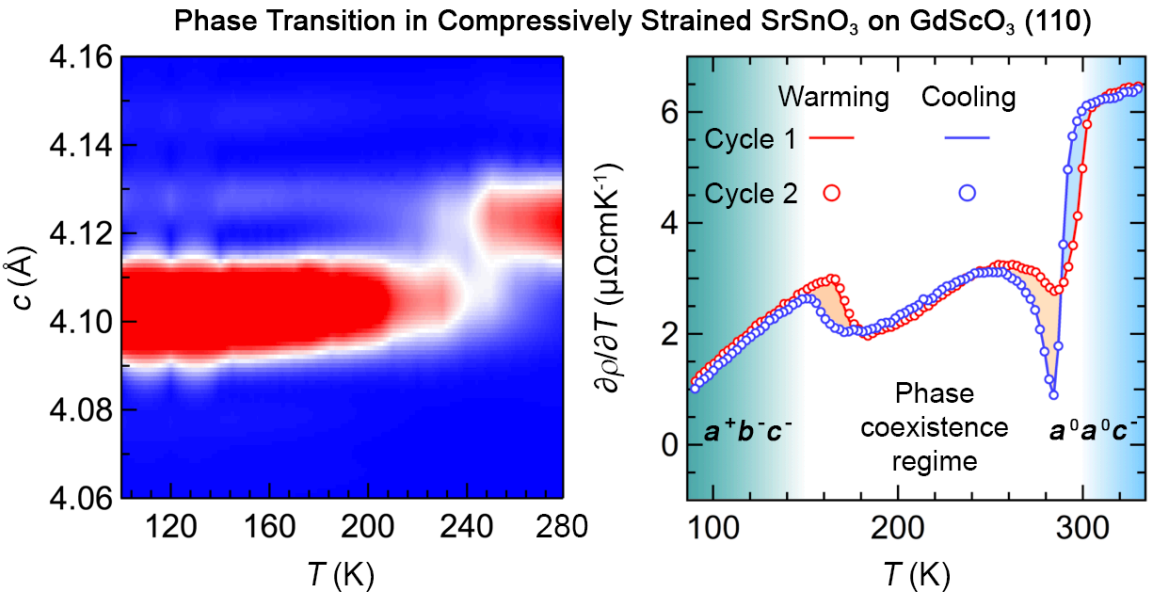
Phase Transition in Compressively Strained SrSnO3 on GdScO3 (110)
4.16
4.14
4.12
4.10
4.08
4.06
c (Å)
120
160
200
240
280
T (K)
∂ρ/∂T (μΩcmK-1)
6
4
2
0
Warming
Cooling
Cycle 1
Cycle 2
a+b-c-
Phase
coexistence
regime
a0a0c-
100
200
300
T (K)

Supporting Information

Engineering $SrSnO_3$ Phases and Electron Mobility at Room Temperature Using Epitaxial Strain

Tianqi Wang[1, *, †], Abhinav Prakash[1, *, †], Yongqi Dong[2, 3, 5], Tristan Truttmann[1], Ashley Bucsek[4], Richard James[4], Dillon D. Fong[2], Jong-Woo Kim[3], Philip J. Ryan[3], Hua Zhou[3], Turan Birol[1], and Bharat Jalan[1,*]

[1]Department of Chemical Engineering and Materials Science
University of Minnesota,
Minneapolis, Minnesota 55455, USA

[2]Materials Science Division, Argonne National Laboratory,
Argonne, Illinois 60439, USA

[3]Advanced Photon Source, Argonne National Laboratory,
Argonne, Illinois 60439, USA

[4]Department of Aerospace Engineering and Mechanics
University of Minnesota
Minneapolis, Minnesota 55455, USA

[5]National Synchrotron Radiation Laboratory, University of Science and Technology of China,
Hefei, Anhui 230026, China

† Equal contributing authors

a) Corresponding authors: wang3769@umn.edu, praka019@umn.edu, and bjalan@umn.edu

A. Stability of different polymorphs of $SrSnO_3$ under various biaxial strain using density functional theory

Epitaxial strain can stabilize new phases. Using DFT calculations (refer to the method section in the main text for details), figure S1 shows the calculated free energies of $SrSnO_3$ phases with different space groups and tilt patterns as a function of in-plane biaxial strain i.e., constrained in-plane lattice parameter. With increasing compressive strain or decreasing in-plane lattice parameter, tetragonal phase with *I4/mcm* space group and $a^0a^0c^-$ pattern possess lowest energy and is most stable.

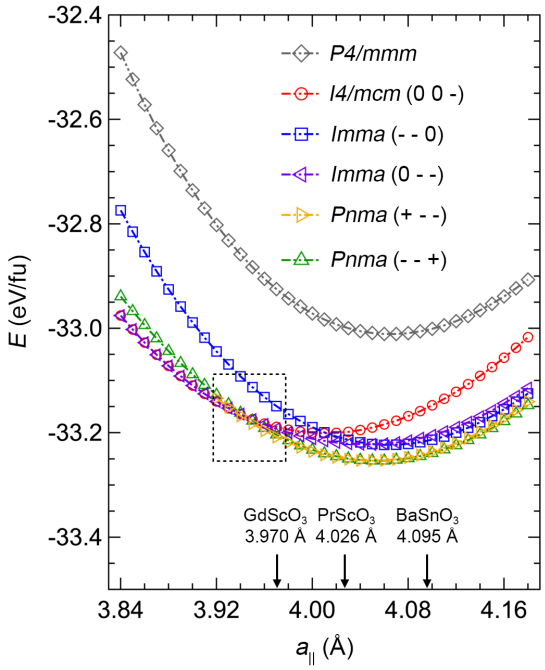

Figure S1: Phase stability diagram. Free energies of different $SrSnO_3$ polymorphs as a function of constrained in-plane lattice parameters. The arrows mark the lattice parameters corresponding to the three substrates used in this study – (110) $GdScO_3$, (110) $PrScO_3$, and (001) $BaSnO_3$. The box highlights a regime where crossover of stable phases happens under compressive strain.

B. Calculated lattice parameters for fully-coherent films on different substrates using theoretical elastic constants

Table S1: **Calculated lattice parameter of different phases under biaxial strain.** The expected out-of-plane lattice parameters of SSO films on different substrates for the three non-cubic polymorphs of SSO (bulk lattice parameters and tilt patterns are shown below). Out-of-plane lattice parameters are calculated assuming fully-coherent films and using theoretical elastic tensors for two different cases of *c*-axis in-plane and out-of-plane.[1-2]

Lattice parameter of strained $SrSnO_3$ films with c-axis in-plane

Bulk $SrSnO_3$ phases		orthorhombic space group: *Pnma* Glazer notation: $a^-a^-c^+$ (298-905K) *pseudocubic* a_{pc}=4.035 Å b_{pc}=4.035 Å c_{pc}=4.033 Å		orthorhombic space group: *Imma* Glazer notation: $a^-a^-c^0$ (905-1062K) *pseudocubic* a_{pc}=4.068 Å b_{pc}=4.068 Å c_{pc}=4.057 Å		tetragonal space group: *I4/mcm* Glazer notation: $a^0a^0c^-$ (1062-1295K) *pseudocubic* a_{pc}=4.069 Å b_{pc}=4.069 Å c_{pc}=4.081 Å	
substrate		ε_{ip} (Δa/a.%)	a_{op} (Å) (strained)	ε_{ip} (Δa/a.%)	a_{op} (Å) (strained)	ε_{ip} (Δa/a.%)	a_{op} (Å) (strained)
$GdScO_3$ (110)	a=5.45 Å b=5.75 Å c=7.93 Å	-1.6	4.065	-2.3	4.111	-2.6	4.119
$PrScO_3$ (110)	a=5.61 Å b=5.78 Å c=8.03 Å	-0.2	4.038	-0.9	4.085	-1.2	4.093
$BaSnO_3$/ $SrTiO_3$ (001)	a=4.095 Å b=4.095 Å c=4.130 Å	+1.5	4.006	+0.8	4.052	+0.5	4.060

Lattice parameter of strained $SrSnO_3$ film with c-axis out-of-plane

substrate		ε_{ip} (Δa/a.%)	a_{op} (Å) (strained)	ε_{ip} (Δa/a.%)	a_{op} (Å) (strained)	ε_{ip} (Δa/a.%)	a_{op} (Å) (strained)
$GdScO_3$ (110)	a=5.45 Å b=5.75 Å c=7.93 Å	-1.6	4.063	-2.4	4.103	-2.4	4.128
$PrScO_3$ (110)	a=5.61 Å b=5.78 Å c=8.03 Å	-0.2	4.037	-1.0	4.076	-1.1	4.101
$BaSnO_3$/ $SrTiO_3$ (001)	a=4.095 Å b=4.095 Å c=4.130 Å	+1.5	4.004	+0.7	4.044	+0.6	4.068

C. Comparison of $SrSnO_3$ films of different thicknesses on $GdScO_3$ (110)

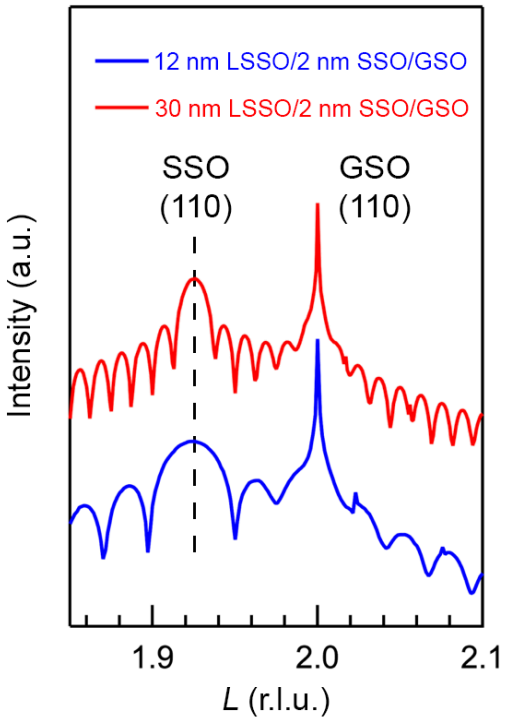

Figure S2: **Wide-angle x-ray diffraction.** Comparison of wide-angle x-ray 2θ-ω scans around (002) reflection for a 12 nm La-doped SSO/2 nm SSO/$GdScO_3$ (GSO) (110) and 30 nm La-doped SSO/2 nm SSO/$GdScO_3$ (GSO) (110) films showing an identical out-of-plane lattice parameter regardless of the film thickness.

D. Half-order diffraction analysis

Synchrotron-based, half-order Bragg peak analyses were performed to determine SnO_6 tilt patterns, which are unique for the three polymorphs of SSO.[3] For example, the bulk RT orthorhombic phase (*Pnma)* exhibits the $a^-a^-c^+$ tilt pattern, whereas the high-temperature orthorhombic phase (*Imma)* and tetragonal phase (*I4/mcm*) have $a^-a^-c^0$ and $a^0a^0c^-$ tilt patterns, respectively. These tilt patterns are referenced with respect to the orthorhombic unit cell, where the tilt angles α, β, and γ of SnO_6 octahedron are defined along [110], [$\bar{1}$10], [001] directions of the orthorhombic unit cell respectively. Using this analysis, one can apply a few simple rules to

determine the octahedral rotation of the system: (1) even-odd-odd half-order reflections indicate in-phase octahedral rotations (+) whereas odd-odd-odd half-order reflections indicate out-of-phase octahedral rotations (−); (2) an in-phase rotation with even-odd-odd half-order reflections and $k \neq l$ implies an a^+ rotation, and those with odd-even-odd and $l \neq h$, and with odd-odd-even and $h \neq k$ imply b^+ and c^+ rotations, respectively; (3) out-of-phase rotations with odd-odd-odd half-order reflections and $k \neq l$ implies an a^- rotation, and those with $l \neq h$, and $h \neq k$ imply b^- and c^- rotations, respectively. Additionally, using measured and simulated intensities of these half-order reflections, the tilt angles can be quantified. In the discussions that follow, we define tilt patterns of SSO films referenced to the pseudocubic unit cell. For instance, the $a^-a^-c^+$ tilt pattern in the orthorhombic system translates to $a^+b^-c^-$ in the pseudocubic system for a film with the c_{pc} in-plane of the substrate, as illustrated in figure 1a in the main text, while it remains unchanged for the configuration shown in figure 1b. Additionally, if only one set of tilt pattern is observed in the film, that signifies a single domain structure. Identifying the tilt patterns of the films, therefore, also sheds light on whether or not films exhibit single or multiple domains. For thin films, the tilt patterns may also be modified by the symmetry and tilt patterns of the substrate, which we have accounted for in the interpretation of data.

Multiple half-order scans were recorded to retrieve accurate tilt patterns. In the main text, figures 3b, 3c, and 3d show L scans along the (1 $^1/_2$ $^5/_2$), ($^1/_2$ $^1/_2$ $^5/_2$), and ($^3/_2$ $^1/_2$ $^3/_2$) crystal truncation rods, respectively from the SSO film on GSO (110) at 10 K. Based on the rules discussed above, the (1 $^1/_2$ $^5/_2$) peak (Fig. 3b) with even-odd-odd and $k \neq l$ suggests an in-phase rotation (+) along $[100]_{pc}$ of SSO film. Likewise, the ($^1/_2$ $^1/_2$ $^5/_2$) peak (Fig. 3c) is odd-odd-odd, and the inequality $h \neq l$ suggest an out-of-phase rotation (−) along $[010]_{pc}$. In addition, the

appearance of ($^3/_2\ ^1/_2\ ^3/_2$) diffraction peak (Fig. 3d) with odd-odd-odd, and $h \neq k$, suggests the presence of an out-of-phase rotation (−) along the $[001]_{pc}$ of the SSO pseudocubic unit cell. These results thus reveal $a^+b^-c^-$ tilt pattern for SSO film on GSO at 10 K. Similarly, half-order Bragg peak analyses of the SSO film on PSO (110) (figures S3b-d) yields $a^+b^-c^-$ tilt pattern and a single domain structure at both 10 K and 300 K. However, diffraction peaks corresponding to a^+ and b^- are much more intense compared to the film on GSO, suggesting higher tilts angles, α and β in the pseudocubic framework. Noticeably, the observed tilt patterns are similar to that of the underlying GSO (110) or PSO (110) substrates. It is further noted in figure S3a, that SSO film on PSO (110) don't undergo any temperature dependent structural phase transition further providing evidence that RT orthorhombic phase of SSO is stabilized on PSO (110) substrate.

E. Temperature-dependent x-ray diffraction of $SrSnO_3$ film on $PrScO_3$ (110)

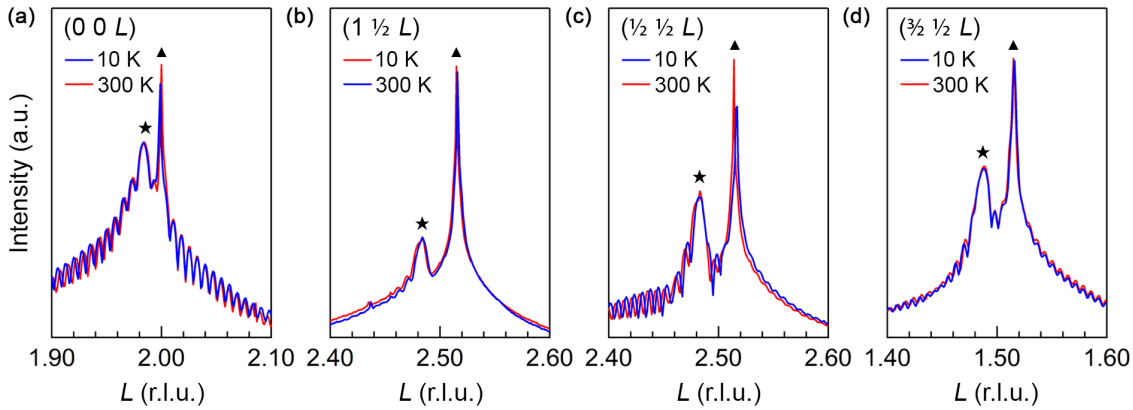

Figure S3: **Half-order diffraction**. (a) Wide-angle scan along (002) reflection, half-order diffraction scans about (b) ($1\ ^1/_2\ ^5/_2$), (c) ($^1/_2\ ^1/_2\ ^5/_2$), and (d) ($^3/_2\ ^1/_2\ ^3/_2$) reflections at 10 K (blue) and 300 K (red) for the film on PSO (110) substrate. No change in half-order peak intensities confirmed room-temperature orthorhombic phase stabilized on $PrScO_3$ with no phase transition at low temperatures. The substrate and film reflections are marked by ▲ and ⋆, respectively.

F. Temperature-dependent x-ray diffraction of $SrSnO_3$ film on $BaSnO_3/SrTiO_3$ (001)

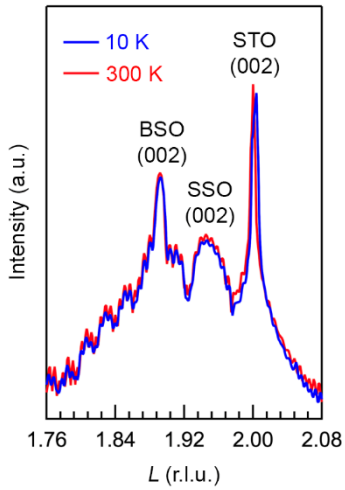

Figure S4: **Effect of tensile strain.** Comparison of wide-angle angle 2θ-ω scans about (002) reflection at 10 K (blue) and 300 K (red) for a 15 nm $SrSnO_3$ film sandwiched between $BaSnO_3$ layers showing no phase transition at low temperatures.

G. Temperature-dependent x-ray diffraction

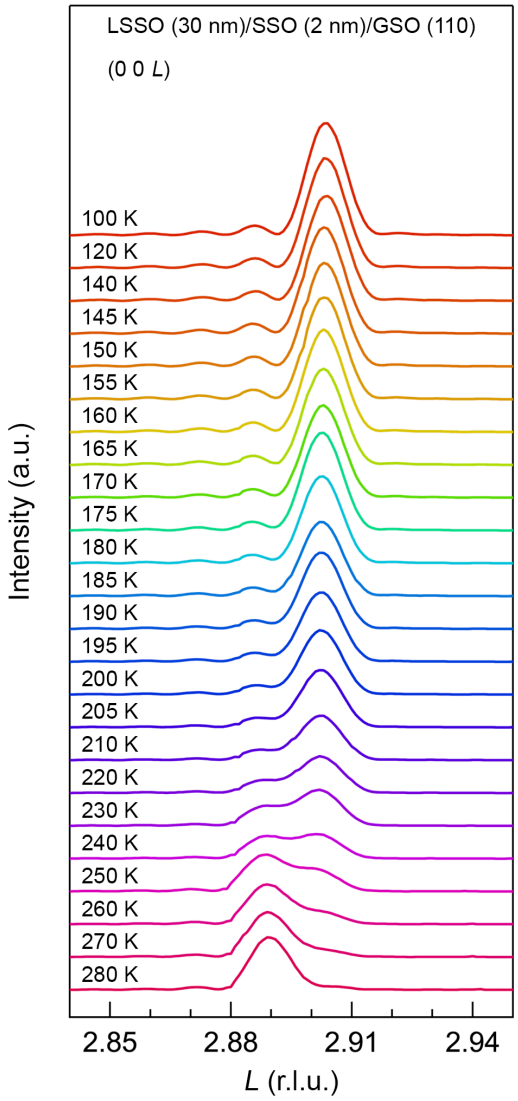

Figure S5: **Temperature-dependent x-ray diffraction.** On-axis x-ray diffraction scans at different temperatures between 100 K and 280 K showing that two phases coexist in nearly 1:1 ratio between 240 K and 250 K. This temperature was precisely calculated to be 243 K from resistivity vs temperature measurements and was marked by an orange arrow in figure 4 of the main text.

H. Qualitative description of large suppression in phase transition temperature

We propose a qualitative explanation for the significant decrease in phase transition temperature as compared to reported bulk values in table S1. This explanation is based on the

minimization of a free energy function. As is conventional with phase transitions, we will assume a multi-well temperature-dependent free-energy function $\varphi(\boldsymbol{F}, \theta)$, where $\boldsymbol{F}$ is the deformation gradient describing some uniform deformation of the lattice and θ is temperature.[4] Figure S6 show a one-dimensional schematic of the free energy function associated with a material that undergoes a ferroelastic phase transition from a high-temperature tetragonal (*I4/mcm*) phase to a low-temperature orthorhombic (*Pnma*) phase. The *y*-axis is the free energy density φ, and the *x*-axis is the deformation gradient $\boldsymbol{F}$ relative to the tetragonal phase. Notice that the central energy well is positioned at the identity tensor, $\boldsymbol{I}$; this is the energy well associated with the tetragonal phase. The energy wells on either side of the tetragonal well are the two orthorhombic wells. There are two wells, because there are two variants associated with the tetragonal-to-orthorhombic phase transition as dictated by the ratio of the number of rotations in the tetragonal point group to the number of rotations in the orthorhombic point group. The deformation gradients, $\boldsymbol{F}_1$ and $\boldsymbol{F}_2$, are the deformation gradients that describe the deformation from the tetragonal lattice to the two variants of the orthorhombic lattice.

First, let us consider an (unconstrained) bulk material that has a transition temperature of $\theta_{C,B}$. This material is free to deform along the *x*-axis in order to minimize the strain-energy. When $\theta > \theta_{C,B}$ (Figure S6a), the minimum energy is located at $\boldsymbol{I}$, so the material will be in the tetragonal phase. When $\theta = \theta_{C,B}$ (Figure S6b), the energy is equally minimized at $\boldsymbol{I}$, $\boldsymbol{F}_1$, and $\boldsymbol{F}_2$, so the material will be a mixture of the tetragonal and orthorhombic phases. When $\theta < \theta_B$ (Figure S6c), the minimum energy is located at $\boldsymbol{F}_1$ and $\boldsymbol{F}_2$, so the material will have completely transformed to the two variants of the orthorhombic phase.

Now, let us consider a thin film grown on a substrate that has a transition temperature of $\theta_{C,F}$. The film is not completely free to deform along the *x*-axis, because it is constrained in-

plane by the substrate. The in-plane constraint imposed by the substrate plus a free out-of-plane deformation can also be described by a deformation gradient, which we will call $\boldsymbol{M}$. $\boldsymbol{M_I}$ is the new deformation gradient associated with the tetragonal phase, and $\boldsymbol{M_{F_1}}$ and $\boldsymbol{M_{F_2}}$ are the new deformation gradients associated with the two variants of the orthorhombic phase. The free out-of-plane deformation can be assumed to be that which minimizes the free energy and can be calculated as a function of the in-plane constraint, e.g., following the approach in Bhattacharya et al.[5] Notice in Figure S6 that the new deformations $\boldsymbol{M_I}$, $\boldsymbol{M_{F_1}}$, and $\boldsymbol{M_{F_2}}$ are located slightly to the sides of the energy well minima. The relative positions of $\varphi(\boldsymbol{M_I}, \theta)$, $\varphi(\boldsymbol{M_{F_1}}, \theta)$, and $\varphi(\boldsymbol{M_{F_2}}, \theta)$ will determine the film phase transition temperature $\theta_{C,F}$. When $\theta > \theta_{C,B}$ (Figure S6a), $\varphi(\boldsymbol{M_I}, \theta) < \varphi\left(\boldsymbol{M_{F_1}}, \theta\right) = \varphi(\boldsymbol{M_{F_2}}, \theta)$. Like the bulk material, the film will be in the tetragonal phase at this temperature. When $\theta = \theta_{C,B}$ (Figure S6b), $\varphi(\boldsymbol{M_I}, \theta) < \varphi\left(\boldsymbol{M_{F_1}}, \theta\right) = \varphi(\boldsymbol{M_{F_2}}, \theta)$. While the bulk material would be in the midst of transformation, the film is still stable in the tetragonal phase at this temperature. It is only at some lower temperature $\theta_{C,F} = \theta < \theta_{C,B}$ (Figure S6c) that $\varphi(\boldsymbol{M_I}, \theta) = \varphi\left(\boldsymbol{M_{F_1}}, \theta\right) = \varphi(\boldsymbol{M_{F_2}}, \theta)$ and the film is ready to transition to the orthorhombic phase.

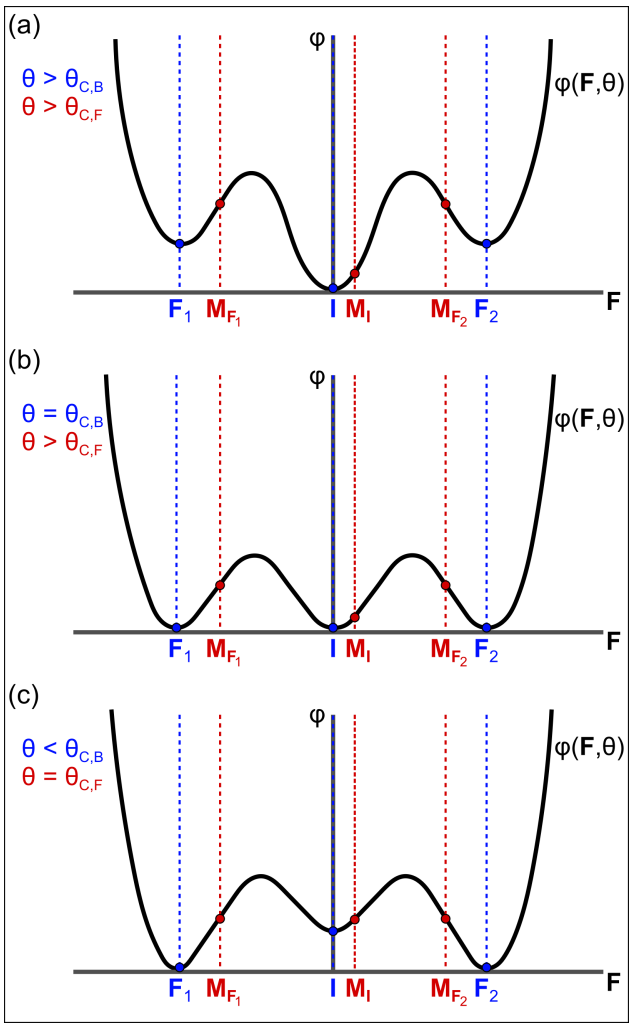

Figure S6: A one-dimensional schematic illustration of the effect of constraint imposed by a substrate on the phase transition temperature. While a bulk material with this free energy function would be in the high-temperature phase in (a), mixed phase at (b), and in the low-temperature phase in (b), a constraint imposed by a substrate will affect the stability of the phases at each temperature range. In this example, the high-temperature phase is stable at a larger range of temperatures (a,b), and the phase transformation does not occur until (c).

This discussion is a qualitative illustration of how substrate misfit can change the phase transition temperature of a thin phase-transforming film. This particular explanation was constructed in order to understand the dramatic decrease observed for the tetragonal-to-orthorhombic phase transformation in $SrSnO_3$, but the same explanation can be used to

understand why an increase in phase transition temperature has been observed for other film and substrate combinations.[6] The direction and degree of the change in phase transition temperature will depend on the free energy function and the film and substrate lattice parameters. Although we have made lattice parameter measurements for this material, a free energy function for this particular phase transformation and material system has yet to be formulated. A more quantitative analytical explanation of the effect of substrate misfit on phase transition temperatures is part of ongoing research and will be presented elsewhere.

References:

1. Glerup, M.; Knight, K. S.; Poulsen, F. W., High Temperature Structural Phase Transitions in $SrSnO_3$ Perovskite. *Mater. Res. Bull.* **2005,** *40* (3), 507.
2. Ghebouli, B.; Ghebouli, M. A.; Chihi, T.; Fatmi, M.; Boucetta, S.; Reffas, M., First-principles Study of Structural, Elastic, Electronic and Optical Properties of $SrMO_3$ (M=Ti and Sn). *Solid State Commun.* **2009,** *149* (47), 2244.
3. May, S. J.; Kim, J. W.; Rondinelli, J. M.; Karapetrova, E.; Spaldin, N. A.; Bhattacharya, A.; Ryan, P. J., Quantifying Octahedral Rotations in Strained Perovskite Oxide Films. *Phys. Rev. B* **2010,** *82* (1), 014110.
4. Ball, J. M.; James, R. D., Fine Phase Mixtures as Minimizers of Energy. *Arch. Ration. Mech. An.* **1987,** *100* (1), 13.
5. Bhattacharya, K.; James, R. D., A Theory of Thin Films of Martensitic Materials with Applications to Microactuators. *J. Mech. Phys. Solids.* **1999,** *47* (3), 531.
6. Haeni, J. H.; Irvin, P.; Chang, W.; Uecker, R.; Reiche, P.; Li, Y. L.; Choudhury, S.; Tian, W.; Hawley, M. E.; Craigo, B.; Tagantsev, A. K.; Pan, X. Q.; Streiffer, S. K.; Chen, L. Q.; Kirchoefer, S. W.; Levy, J.; Schlom, D. G., Room-Temperature Ferroelectricity in Strained $SrTiO_3$. *Nature* **2004,** *430*, 758.